OPTICS

Room-temperature on-chip orbital angular momentum single-photon sources

Cuo Wu[1,2]†, Shailesh Kumar[2]†, Yinhui Kan[2,3], Danylo Komisar[2], Zhiming Wang[1], Sergey I. Bozhevolnyi[2], Fei Ding[2]*

On-chip photon sources carrying orbital angular momentum (OAM) are in demand for high-capacity optical information processing in both classical and quantum regimes. However, currently exploited integrated OAM sources have been primarily limited to the classical regime. Here, we demonstrate a room-temperature on-chip integrated OAM source that emits well-collimated single photons, with a single-photon purity of $g^{(2)}(0) \approx 0.22$, carrying entangled spin and OAM states and forming two spatially separated entangled radiation channels with different polarization properties. The OAM-encoded single photons are generated by efficiently outcoupling diverging surface plasmon polaritons excited with a deterministically positioned quantum emitter via Archimedean spiral gratings. Our OAM single-photon source platform bridges the gap between conventional OAM manipulation and nonclassical light sources, enabling high-dimensional and large-scale photonic quantum systems for quantum information processing.

INTRODUCTION

Angular momentum that includes the spin angular momentum (SAM) (*1*) related to circular polarizations and the orbital angular momentum (OAM) associated with helical wavefronts is one of the fundamental physical properties of light. In contrast to the SAM that only takes two values of $\pm\hbar$, the OAM can carry discrete angular momenta of $\ell\hbar$ (*2–4*), where ℓ is an unbound integer corresponding to the topological charge and $\hbar$ is the reduced Planck constant. The possibility of generating an infinite number of states characterized by different OAMs opens up an unprecedented opportunity for high-capacity information processing in both classical and nonclassical regimes. Typically, OAM beams are generated by combining external light sources and extra phase transformers, including either bulk optical components such as computer-generated holograms (*5*, *6*) and spiral phase plates (*7*, *8*), or recently developed compact metasurfaces (*9*, *10*) and whispering-gallery mode resonators (*11*, *12*). Lately, integrated chip-scale microlasers have been extensively investigated for internally excited vortex beams with high purity (*13–18*).

Despite certain achievements, the insofar demonstrated on-chip OAM sources are limited to the classical regime, while compact quantum sources of OAM encoded single photons still remain largely unexplored. To realize quantum sources of photons carrying OAM, separate single photons from spontaneous parametric down-conversion (SPDC) process are combined with extra phase modulators (*19*, *20*), resulting in bulky configurations and additional losses. SPDC-based single-photon sources are inherently probabilistic, exhibiting an intrinsic trade-off between their efficiency and photon purity, a circumstance that limits their potential for being exploited in large-scale and high-dimensional photonic quantum systems. Very recently, solid-state sources for single photons with OAM

have been realized using epitaxial quantum dots embedded in microring resonators cooled to a temperature of 30 K (*21*), which restricts the practical applications at room temperature. Room-temperature on-chip integrated sources of single photons carrying OAM states have remained so far elusive while being in demand for high-capacity quantum information processing to meet requirements of increasing both photon states and entanglement dimensionality.

Here, we use deterministically positioned nanodiamonds (NDs) containing individual nitrogen-vacancy (NV) centers (ND-NVs) as single quantum emitters (QEs) to spontaneously trigger collimated single photons carrying SAM and OAM superposition states, which is efficiently outcoupled by QE-excited diverging surface plasmon polaritons (SPPs) with an Archimedean spiral grating (*22–24*) atop a dielectric-spacer–coated silver substrate. The considered configuration enables room-temperature generation of oppositely spinning photons carrying the conserved total angular momentum and propagating in spatially separated entangled radiation channels.

RESULTS

Design principle of on-chip OAM sources

The operation of our OAM single-photon source is schematically visualized using layer-by-layer representation in Fig. 1A. A preselected ND-NV with desired single QE characteristics and having the main contribution of the radiative transition dipole moment normal to the surface (i.e., along the z axis) is deterministically located in the center of an Archimedean spiral grating made of hydrogen silsesquioxane (HSQ) atop a thin silica (SiO_2) spacer film supported by a silver (Ag) substrate. This preferable dipole orientation is ensured by selecting those ND-NVs that luminesce most strongly when being illuminated with a tightly focused radially polarized laser beam, which produces a strong normal (to the surface) electric field component E_z of the pump beam in the focal plane (*25*). Consequently, upon excitation of thus selected ND-NV with a tightly focused radially polarized pump laser beam (excitation not shown in the schematic), the ND-NV transition dipole along the z axis is the main source of radiation radiating into cylindrically diverging (i.e., radial) SPPs supported by the composite air-SiO_2-Ag
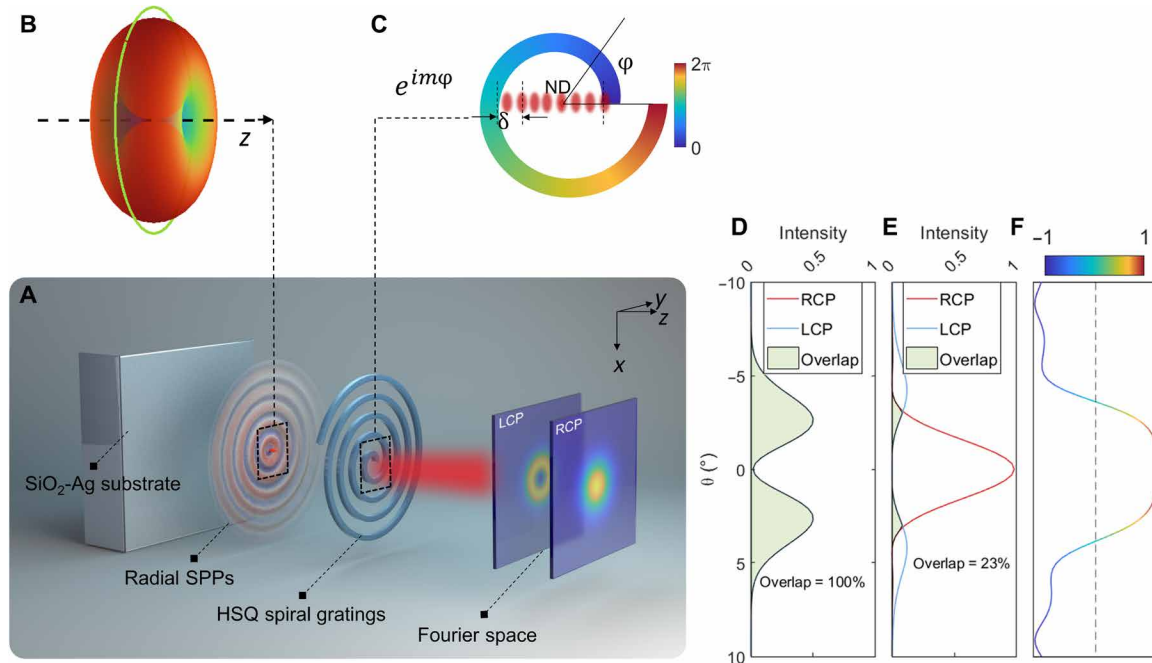
Fig. 1. Design of the collimated OAM single-photon source. (**A**) Schematic of the OAM single-photon source operation in layer-by-layer representation: a SiO$_2$-coated Ag substrate, supporting radial SPPs excited by a QE z-oriented dipole; an HSQ spiral grating, outcoupling SPPs into a well-collimated photon stream; and decomposed far-field RCP and LCP intensity profiles, from left to right, respectively. (**B**) Three-dimensional rendering of the electric field radiation of a z-oriented dipole. (**C**) Analytical azimuthal phase distribution generated due to the propagation and scattering of radial SPPs on the first winding of the HSQ spiral. (**D** and **E**) Analytical cross-sectional profiles of far-field RCP and LCP components produced with radial SPPs being outcoupled by a bullseye grating (D) and one-arm CCW spiral grating (E). The intensity overlap between the RCP and LCP components is 100 and 23%, respectively, demonstrating spatial separation of entangled radiation channels with distinctly different polarization properties. (**F**) Simulated Stokes parameter S_3 of RCP (+1) and LCP (−1) components in the total field.

interface (*25, 26*). Note that it is only the SPP in-plane components that can be efficiently outcoupled into far-field radiation along the normal to the surface direction. These SPP in-plane components can be expressed in the propagation plane as follows, considering only the main terms at distances far away from the source point (*27*): $\vec{E}_{spp} = \frac{\exp(i k_{spp} r)}{\sqrt{r}} \binom{\cos\varphi}{\sin\varphi}$, where φ is the azimuthal angle, r is the distance to the source point, and k_{spp} is the SPP propagation constant (Fig. 1, A and B). After propagating over an azimuthally varied distance of $r(\varphi) = r_0 + |m| \frac{\lambda_0}{n_{spp}} \frac{\varphi}{2\pi}$ ($0 \ll \varphi < 2N\pi$), the SPP in-plane components interact with the Archimedean spiral grating that subsequently scatters SPPs into collimated single photons propagating away from the surface and carrying a spiral phase profile of $\delta(\varphi) = n_{spp} \frac{2\pi}{\lambda_0} r(\varphi) = m\varphi + \delta_c$, where r_0 is the starting radius, m is the arm number with $m < 0$ for counterclockwise (CCW) spirals, N is the number of spiral windings, λ_0 is the free-space radiation wavelength, $n_{spp} = \frac{\lambda_0}{2\pi} \text{Re}(k_{spp})$ is the effective SPP mode index, and $\delta_c = n_{spp} \frac{2\pi}{\lambda_0} r_0 + \delta_0$ is a constant phase term including the phase shift δ_0 during the SPP scattering. Hence, the polarization state of generated single photons in the far field can be represented as the OAM superposition state in the circularly polarized (CP) basis (note S1)

$$|\psi_m\rangle = \frac{1}{\sqrt{2}}(|R\rangle |\ell_R = m + 1\rangle - |L\rangle |\ell_L = m - 1\rangle) \quad (1)$$

showing unambiguously that the right CP [RCP, $|R\rangle$] and left CP [LCP, $|L\rangle$] OAM beams with topological charges of $\ell_R = m + 1$ and

$\ell_L = m − 1$, respectively, are generated simultaneously, forming a pair of entangled states composed of different SAM and OAM with the total angular momentum being conserved (fig. S1).

If the CCW spiral grating has only one arm (i.e., $m = −1$), then the accumulated phase variation δ is continuously changed within the full 2π range with respect to the azimuthal angle φ rotating from 0 to 2π for scattered electric fields that originate from the spiral head to its tail (Fig. 1C). The corresponding far-field intensity, which can be found by Fourier transforming the scattered near field, consists of the LCP (with $\ell_L = −2$) and RCP (with $\ell_R = 0$) components featuring, correspondingly, a doughnut profile (intensity vanishes at the center due to the phase singularity) and Gaussian shape (Fig. 1A). Contrary to the SPPs outcoupling with a trivial bullseye (concentric circular) grating producing the far-field intensity pattern with a 100% spatial overlap between the RCP and LCP components (Fig. 1D), the introduced spiral gratings result in spatial separation between the RCP and LCP components, with the intensity overlap of only 23% in the considered one-arm spiral grating (Fig. 1E). The spatial separation of the entangled RCP and LCP radiation channels with the same total angular momentum bears important implications to high-dimensional quantum information processing (*16*). The simulated Stokes parameters further validate the angle-dependent polarization of the outcoupled photons characterized by two entangled, RCP and LCP, states (Fig. 1F), consistent with the cross-sectional profiles in Fig. 1E.

According to the theoretical analysis, we designed three typical CCW Archimedean spiral gratings with $m = −1, −3$, and $−5$ to implement our practical OAM photon sources, ensuring well-defined

far-field radiation patterns and considerably high collection efficiencies (see Materials and Methods, note S2, figs. S2 to S8, and tables S1 and S2). The optimized geometrical parameters of the m-arm concentric spiral are starting radius r_0 = 450 nm, free-space radiation wavelength λ_0 = 670 nm, effective SPP mode index n_{spp} = 1.218, and number of windings N = 9, which is large enough to transform SPPs into outgoing photons. In the case of $|m| > 1$, the adjacent spiral arms are offset with an angle of $\Delta\varphi = 2\pi/|m|$. The concentric HSQ ridges are placed atop an Ag substrate coated with a 20-nm-thin SiO_2 spacer that ensures environmental protection of the Ag substrate, effective coupling of ND-NV radiation into SPPs (26), and a sufficiently long propagation length of SPP (fig. S2). Figure 2A displays the schematic of the spiral gratings and their corresponding analytical phase distributions, indicating m-fold 2π phase variation along the azimuthal direction. The performance of the proposed OAM photon sources was first investigated with simulations where the QE was modeled as a z-oriented electric dipole and positioned 30 nm away from the SiO_2 spacer. After interaction with Archimedean spiral gratings (fig. S4), the radial SPPs excited from QE radiation are converted into well-collimated outgoing photons carrying different SAM and OAM and concentrated around the center in the far field (Fig. 2B, note S3, and fig. S5). As a result, the simulated collection efficiency through an objective with a numerical aperture (NA) of 0.9 exceeds 97%, even for the most divergent LCP OAM light with $\ell_L = -6$ achieved with the five-arm spiral (fig. S6). With arm number varied from −1 to −5, the LCP beam maintains a

directional doughnut shape with the divergence angle increased, while the RCP beam changes from Gaussian-shaped to doughnut-shaped, whose topological charges can be directly recognized from the simulated phase windings in the CP basis (Fig. 2C and fig. S9). Because the RCP and LCP components share almost 50/50 power of the out-coupled QE radiation (fig. S3), the OAM beams with higher topological charges look dimmer. Following simulations, the OAM photon sources were fabricated with NDs containing multiple NV centers as a conceptual demonstration based on the equivalence between multiple and single ND-NVs by using a combined process including thin-film deposition, spin-coating, and electron-beam lithography (EBL) (see Materials and Methods along with figs. S11 to S13). Figure 2 (D to F) shows the top-view scanning electron microscopy (SEM) images of the HSQ spiral gratings with ND-NVs precisely positioned. Compared to semiconductor microring lasers (28) or metasurface-assisted surface-emitting lasers (29) and SAM single-photon sources (30, 31), we directly pattern HSQ resists to make spiral gratings with an extremely small vertical feature size of only 180 nm, thereby avoiding the complex etching and multiple steps of alignment that may change or damage the emission property of the QEs.

Experimental demonstration of OAM sources with multiple and single NV centers

To attain the designed OAM emission, we optically pumped the selected ND-NVs with a tightly focused radially polarized beam at a wavelength of 532 nm to produce a strong longitudinal electric field
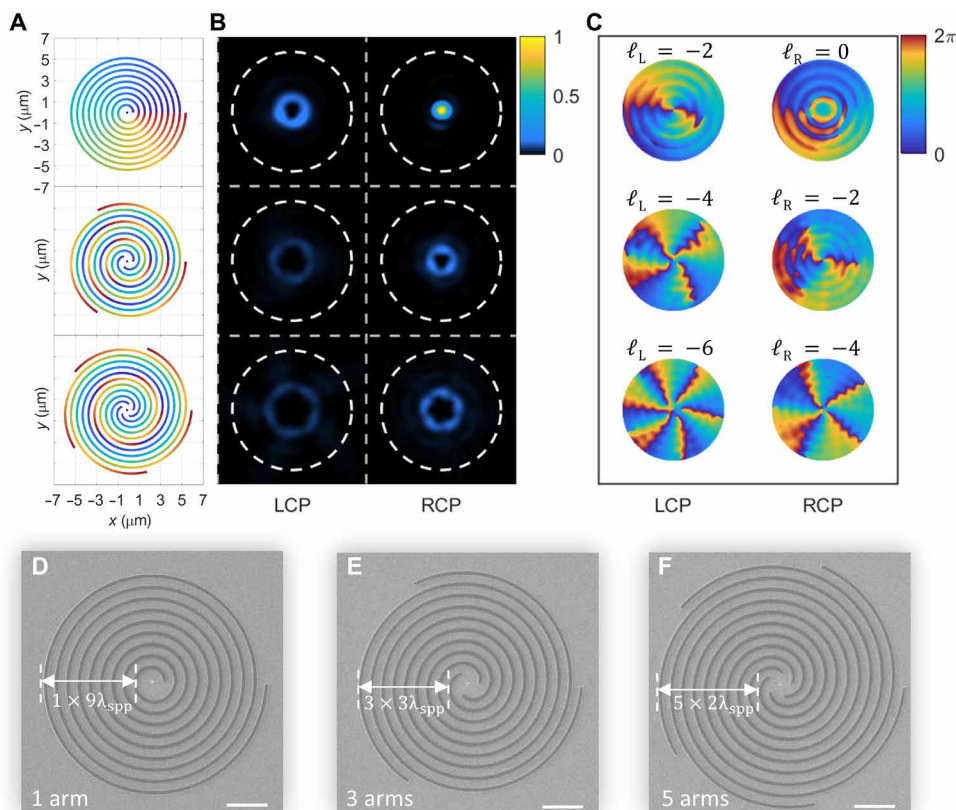

Fig. 2. Simulation of the collimated OAM photon sources. (**A**) Schematic of the spiral gratings and their corresponding analytical phase distributions with arm number of $m = -1, -3$, and -5 from top to bottom, respectively. (**B**) Decomposed far-field LCP and RCP intensity profiles normalized to the one-arm spiral grating. The white dashed circles denote the collection angle with numerical aperture (NA) = 0.2. (**C**) Simulated phase windings in the far field for corresponding configurations. (**D** to **F**) SEM images of the fabricated OAM photon sources with arm number of $m = -1, -3,$ and -5. $\lambda_{spp} = \frac{\lambda_0}{n_{spp}}$ is the SPP wavelength. Scale bars, 2 μm.

component E_z at the sample surface (see Materials and Methods along with fig. S14), which can selectively excite the z component of the transition dipole in ND-NVs, mimicking the simulation condition (*32–34*). In the Fourier plane, a linear polarizer (LP) and a quarter-wave plate (QWP) were used to decompose the far-field radiation into the CP basis, where the fast axis of the QWP is set to be ±45° while the LP is vertically placed. When the QWP is −45°-oriented, the projected LCP components all have doughnut shapes spatially expanding with the increased arm number (Fig. 3A). Specifically, the measured divergence angles are θ_{div} = 4.37°, 7.93°, and 10.50° for the spirals with arm number of m = −1, −3, and −5, respectively, consistent with analytical calculations. With the QWP rotated to 45°, a Gaussian-shaped (ℓ_R = 0 with the main lobe at θ = 0°) and other two doughnut-shaped (ℓ_R = −2 with θ_{div} = 4.54° and ℓ_R = −4 with θ_{div} = 8.64°, respectively) RCP beams are observed with the increase arm number (Fig. 3B). By integrating the far-field intensities in the CP basis, the intensity fractions between the RCP and LCP components are 48/52, 49/51, and 51/49, respectively, approaching the theoretically calculated and simulated values (fig. S3).

By using specific NDs with a small fraction containing single NV centers, collimated OAM single-photons are presented at room temperature with one-arm HSQ spiral grating. Compared to NDs with multiple NV centers, these single-NV NDs have smaller diameters and lower scattering cross sections, which can be deterministically located with fluorescence images (fig. S16, middle). After locating several fluorescent ND-NV candidates with a strong out-of-plane radiative transition dipole component indicated by strong luminescence when being illuminated with a tightly focused radially polarized pump beam, a Hanbury Brown and Twiss interferometer was used to determine the ND-NV with single QE characteristics. Before fabrication (the uncoupled bare single ND-NV), the fitted second-order intensity correction function $g^2(0)$ of the selected single-vacancy ND is only ~0.16, indicating high single-photon purity. As anticipated, the far-field intensities projected to CP basis are homogeneously distributed with near-identical patterns in the Fourier plane, resulting from the direct far-field radiation from the QE with the dipole moment normal to the surface (fig. S16, top) (*34–36*). After fabrication of the one-arm HSQ spiral grating around the pre-characterized ND containing a single NV center (the coupled configuration), the autocorrelation $g^2(0)$ is slightly increased to ~0.22, maintaining the intrinsic single-photon feature at room temperature (fig. S16, bottom). In addition, the HSQ spiral grating also provides weak backscattering (second-order Bragg reflection) for the ND-NV, which slightly enhances the emission and shortens the lifetime (fig. S17, A and B) (*37*). Afterward, well-collimated single-photon out-of-plane emission is formed due to the interaction between radial SPPs and the introduced spiral grating, which does not require cryogenic environment and multimode interference (*21*). Impressively, the decomposed LCP beam carries OAM with a topological charge of ℓ_L = −2 and features a doughnut shape, while the RCP component has pure SAM and exhibits a Gaussian distribution (Fig. 4, A and B). The measured mode purities as defined in (*28*) of the decomposed LCP and RCP components after phase-demodulated by a spatial light modulator (SLM) are found to be 62.0 and 66.6%, respectively (note S4 and figs. S20 and S21). Compared to the simulated values (fig. S22), the mode purity degradation is mainly associated with the broadband spontaneous emission of the ND-NV that are not spectrally filtered to ensure a sufficient signal-to-noise ratio after the mode projection by the SLM that intrinsically
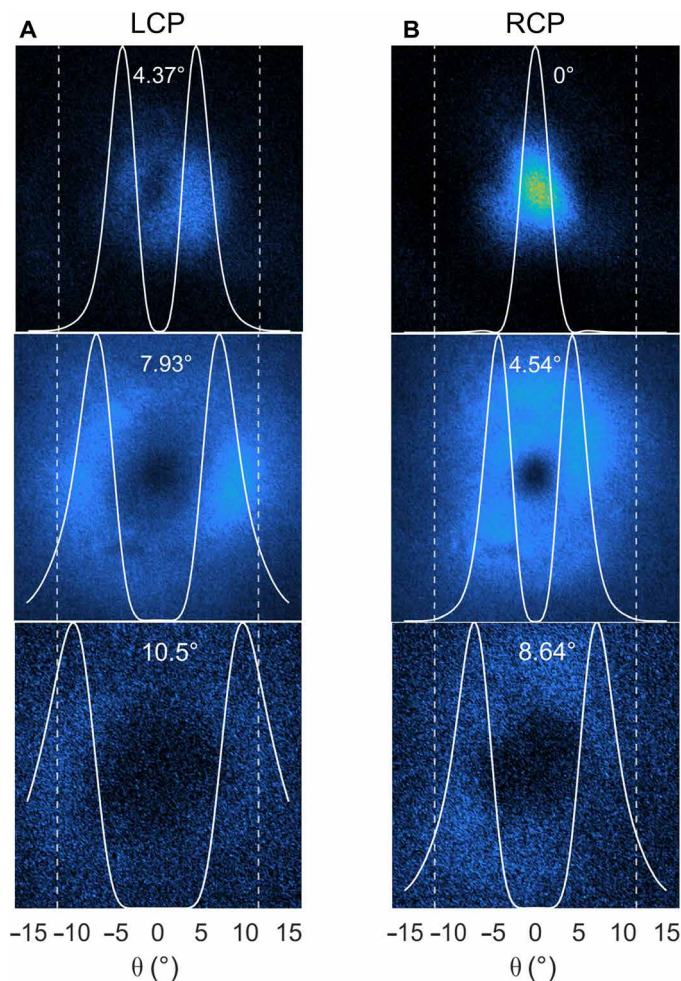

Fig. 3. Experimental demonstration of the collimated OAM photon sources. (**A** and **B**) Measured far-field LCP (A) and RCP (B) intensity patterns as a function of the collection angles. Superimposed white curves are the analytically calculated cross-sectional profiles along the x axis, while dashed lines indicate the collection angle with NA = 0.2. The numbers denote the positions of peak in the respective figure panels.

suffers from optical aberration (e.g., chromatic aberration and distortion) when multiple wavelengths are involved. Here, the degradation can be possibly addressed by using group IV color centers in NDs with sharp and strong zero-phonon lines (*38*).

Entanglement between SAM and OAM states

The generated single photons carry SAM and OAM superposition states and form two spatially separated entangled radiation channels with distinctly different polarization properties without any external quantum sources (*19*), providing multiple degrees of freedom to encode high-capacity information on a single photon for advanced quantum information processing (*19, 30, 39–41*). First, the superposed polarized radiation channels are still correlated. As shown in Fig. 4D, a polarizing beam splitter (PBS) was used to split single photons into two separate channels with specific polarization states. The LCP channel and RCP channel carrying OAM and SAM are antibunching with $g^2(0) \approx 0.15$ (Fig. 4C). To show the entanglement between SAM and OAM states and validate the Bell state of
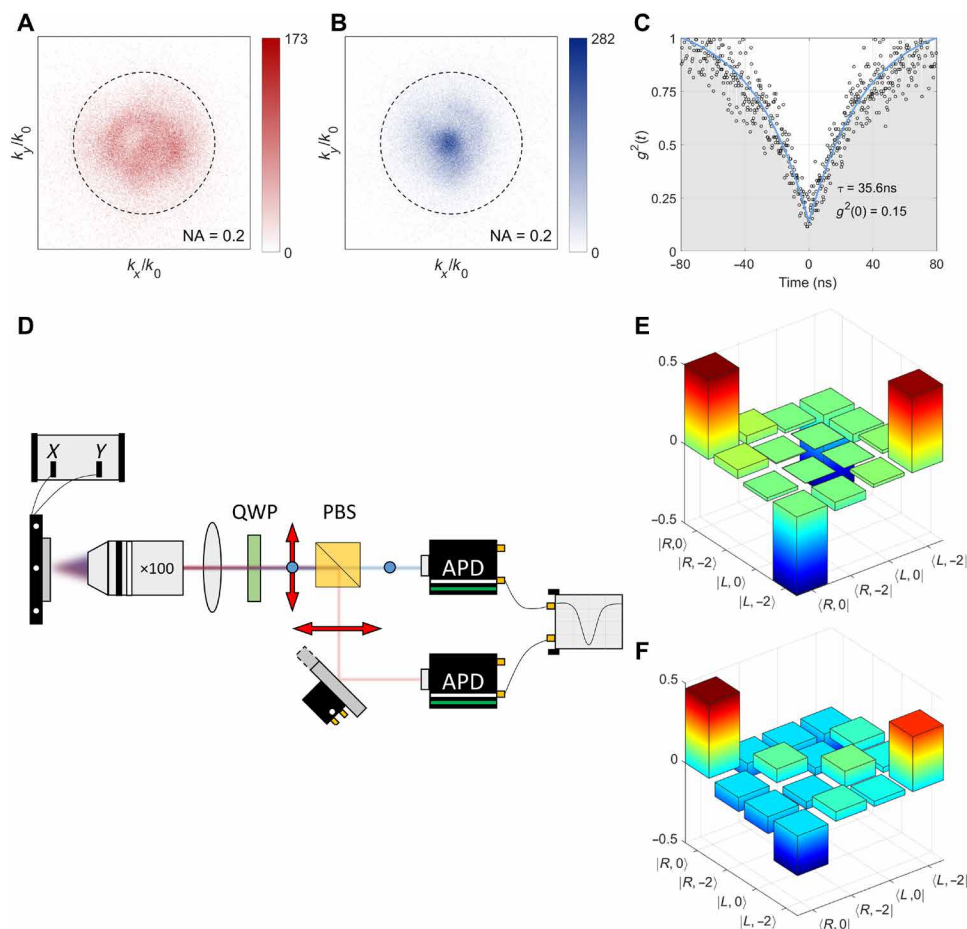
Fig. 4. Experimental demonstration of the collimated OAM single-photon source. (**A** and **B**) Measured far-field LCP (A) and RCP (B) intensity patterns with the single-photon source. (**C**) Measured correlation between LCP and RCP channels. (**D**) Simplified representation of a modified Hanbury Brown and Twiss setup for correlation measurement between RCP and LCP channels. (**E** and **F**) Simulated (E) and experimental (F) density matrices for the Bell state $|\psi\rangle$ on single photons.

the generated single photons, we performed full quantum state tomography to recover the density matrix by conducting 16 projection measurements with different polarization and OAM bases (note S5, fig. S20, and table S3) (*42, 43*). The simulated and measured density matrices of the Bell state $|\psi\rangle = \frac{1}{\sqrt{2}}(|R\rangle|\ell_R = 0\rangle - |L\rangle|\ell_L = -2\rangle)$ are well recovered (Fig. 4, E and F), with fidelities (note S5) approaching 0.991 and 0.656, respectively, indicating the entanglement between SAM and OAM states. Noticeably, the deteriorated fidelity in the experiment that is linked to the measured mode purities can be also efficiently improved with group IV color centers in NDs (*38*). The emitted single photons carrying entangled SAM and OAM states are highly stable in tracing duration up to 20 min without any operation (fig. S17C). Despite moderate mode purities and fidelity, this ultrathin planar device effectively reduces integration complexity and emits well-collimated high-purity single photons carrying SAM and OAM superposition states at room temperature.

DISCUSSION
We have demonstrated a room-temperature on-chip integrated OAM single-photon source that emits well-collimated and high-purity

single photons carrying entangled SAM and OAM states. The OAM single-photon source is realized by efficiently extracting in-plane diverging SPPs excited from a single ND-NV via the HSQ Archimedean spiral grating that affects spatial phases, which exhibits advantages of surface-confined configuration, reduced fabrication process, and high collection efficiencies. The considered OAM single-photon source is sufficiently robust with respect to the fabrication induced displacement of the ND-NV location at the 20-nm scale (note S6 and fig. S23), which is a typical fabrication accuracy that can be ensured with the standard EBL. We would like to emphasize that similar room-temperature on-chip photon sources with different quantum OAM states can accordingly be demonstrated by using HSQ spiral gratings with arm numbers $|m| > 1$. Our design makes spatially separated entangled radiation channels addressable by directly streaming single photons with entangled SAM and OAM states without any external sources, paving the way for advanced quantum photonic superdense information processing on a chip (*44*). Furthermore, superior OAM single-photon sources with unlocked SAMs and arbitrary topological charges could be targeted by using discrete anisotropic meta-atoms combined with photonic inverse design (*45*). This compact platform is also amenable for developing OAM and time-bin hyperentangled photon pairs by using semiconductor

quantum dots (*46–48*) and opens fascinating perspectives for high-dimensional, large-scale, and integrated photonic quantum systems (*40, 49–51*).

MATERIALS AND METHODS
Numerical simulations
We modeled the performance of OAM sources with different arm numbers in real situations using the finite-difference time-domain method (Lumerical Solutions). In our simulations, a *z*-oriented electric dipole that acts as the QE was placed 30 nm away from a 20-nm-thick SiO₂ spacer on top of a 150-nm-thick Ag substrate. The SiO₂ was regarded as a lossless dielectric with a constant refractive index of $n = 1.45$, while the relative permittivity of Ag was described with the experimental data (*52*). The Archimedean spiral gratings made of HSQ were generated according to the formulas in the Results section, where the refractive index was set to 1.41 at the wavelength of 670 nm based on the spontaneous emission of ND-NVs. Perfectly matched layers were used in the *x*, *y*, and *z* directions to truncate the simulation domain. We optimized the geometry of spirals to be 180 nm in height, 220 nm in width, and 450 nm in starting radius to realize well-defined doughnut patterns in the far field. The SPP wavelength was calculated to be 550 nm based on a filling ratio of 0.4. In the simulation domain, a two-dimensional monitor in the *xy* plane located one wavelength away from the top surface of our device was used to collect electric fields in the near field, which are then transformed into the far-field radiation in the spatial frequency domain. Last, the far fields are decomposed in the CP basis, where the RCP and LCP beams share nearly identical intensities with the fractions approaching 50%, as shown in fig. S3A. Figure S3B displays the simulated topological charges and intensity ratio of RCP and LCP OAM beams as a function of the arm number *m*. Because of the reversal symmetry, similar results can be observed once the rotation of the spiral gratings is switched from CCW to clockwise.

Device fabrication
As discussed in the Results section, the fabrication of the OAM sources is feasible, which is based on the combined techniques of thin-film deposition, spin-coating, and EBL, without any etching. Figure S11 illustrates the main workflows of the fabrication process. First, the gold (Au) alignment markers were defined with the first EBL (fig. S11, A to C). A 3-nm titanium (Ti) layer, a 150-nm Ag layer, and a 1-nm Ti layer were deposited onto a silicon substrate through thermal evaporation successively. Then, a 20-nm SiO₂ spacer was deposited with magnetron sputtering in 1 cycle (fig. S11, A and B). The positive resist polymethyl methacrylate (PMMA) (2% in anisole, MicroChem) with a thickness of 100 nm was spin-coated and baked at 180°C for 2 min. After baking, the PMMA layer was exposed at 30 kV (JEOL-6490 system). After development in the solution of methyl isobutyl ketone (MIBK) and isopropyl alcohol (IPA) of MIBK:IPA = 1:3 for 35 s and rinsing in the solution of IPA for 60 s, a 1-nm Ti adhesion layer and a 35-nm Au layer were subsequently deposited. Last, the Au markers were formed after a liftoff process (fig. S11C). Once the Au markers were defined, a diluted ND solution was spin-coated at 2000 rpm for 60 s on the substrate with markers (fig. S11D), where the spin-coated density of NDs can be controlled by the concentration of the solution. The relative positions of NDs were precisely determined by locating markers around

four corners and fitting the scattering or fluorescence images of NDs (fig. S12). A negative resist HSQ with a concentration of 6 weight % is subsequently spin-coated at 1200 rpm for 60 s to fully cover Au markers and NDs on the substrate (fig. S11E). The designed spiral gratings were patterned around the selected NDs by the second EBL with the precise alignment to the markers, followed by the development in the 25% tetramethylammonium hydroxide solution for 4 min (fig. S11F). The height of the one-arm HSQ spiral is characterized by an atomic force microscope, which is around ~180 nm (fig. S13). The alignment accuracy between HSQ patterns and NDs can be confirmed with SEM images.

Optical characterization
Figure S14 shows the optical setup for the far-field pattern, spectrum, and correlation measurements. A linearly polarized continuous-wave laser (crystal laser) at 532 nm served as the pump laser, whose power was tuned with different neutral density filters for imaging and excitation. The pump laser power could be also continuously adjusted by a half-wave plate and a PBS. After passing through the PBS, the vertically polarized component remained in the optical path. A radial polarization converter (ARCoptix) transformed the linearly polarized light into the radially polarized beam, which was then tightly focused onto the sample plane by a 100× objective with a NA of 0.9 (MPLFLN, Olympus). The fluorescence of the ND was collected by the same objective and filtered with two oppositely faced dichroic mirrors (Semrock). By scanning the sample with a piezo stage, the fluorescence image was constructed by recording the photon counts with a single-photon avalanche photodiode (APD). To measure far-field patterns in the Fourier plane, a flip mirror (FM) and a lens were used to project the back focal plane to the digital camera (Hamamatsu). Figure S15 shows the projected total far-field patterns of the fabricated OAM sources composed of NDs containing multiple NVs and HSQ spiral gratings with different arm numbers without any filters, which are consistent with the simulation results in fig. S5. With a broadband QWP mounted on a programmable controlled rotation stage and a LP vertically orientated, the far-field radiation was decomposed into the CP basis. By flipping the FM down, the ND emission went through a beam splitter and its photon counts were collected by two APDs, forming a Hanbury Brown and Twiss interferometer for second-order intensity correlation or lifetime measurement. As NV center is a three-level system, the correlation between two APDs can be described as

$$g^2(\tau) = 1 + c_2 e^{-\frac{\tau}{\tau_2}} + c_3 e^{-\frac{\tau}{\tau_3}} \tag{2}$$

where $c_{2,3}$ and $\tau_{2,3}$ are the coefficients and decay times, respectively. The measured $g^2(0)$ of the selected single-vacancy ND before coupled to the spiral is only ~0.16, indicating high single-photon purity. In this case, the total far-field intensities of the single photon emission are uniformly distributed in the Fourier plane (fig. S16A). With polarization projection by using the QWP and LP, we can observe evenly distributed RCP and LCP components contributed from radial SPPs (fig. S16, B and C). After fabricating the one-arm HSQ spiral, in the fluorescence map, there appears a disk contour around the selected ND, which is associated with the fluorescence from the fabricated HSQ spiral grating and, in turn, demonstrates the precise alignment and high fabrication quality. After coupling, the spontaneous emission of ND is enhanced in spectrum and shortened in lifetime due to the feedback of the HSQ spiral grating

(fig. S17, A and B). We also keep pumping our OAM single-photon emitter for 20 min without any operation. Overall, the count trace shows highly stable emission except for the slight decrease in counts due to the laser shifting and defocusing from intrinsic displacement and vibration in the setup as well as the blinking arising from switching of charged states between NV^- and NV^0 in NDs (fig. S17C).

SUPPLEMENTARY MATERIALS

Supplementary material for this article is available at https://science.org/doi/10.1126/sciadv.abk3075

REFERENCES AND NOTES

1. P. Lodahl, S. Mahmoodian, S. Stobbe, A. Rauschenbeutel, P. Schneeweiss, J. Volz, H. Pichler, P. Zoller, Chiral quantum optics. *Nature* **541**, 473–480 (2017).
2. C.-W. Qiu, Y. Yang, Vortex generation reaches a new plateau. *Science* **357**, 645 (2017).
3. Y. Shen, X. Wang, Z. Xie, C. Min, X. Fu, Q. Liu, M. Gong, X. Yuan, Optical vortices 30 years on: OAM manipulation from topological charge to multiple singularities. *Light Sci. Appl.* **8**, 90 (2019).
4. Q. Zhan, Cylindrical vector beams: From mathematical concepts to applications. *Adv. Opt. Photon.* **1**, 1–57 (2009).
5. G. Li, B. P. Clarke, J.-K. So, K. F. MacDonald, N. I. Zheludev, Holographic free-electron light source. *Nat. Commun.* **7**, 13705 (2016).
6. J. Lin, P. Genevet, M. A. Kats, N. Antoniou, F. Capasso, Nanostructured holograms for broadband manipulation of vector beams. *Nano Lett.* **13**, 4269–4274 (2013).
7. Z. E. Bomzon, G. Biener, V. Kleiner, E. Hasman, Radially and azimuthally polarized beams generated by space-variant dielectric subwavelength gratings. *Opt. Lett.* **27**, 285–287 (2002).
8. K. M. Dorney, L. Rego, N. J. Brooks, J. San Román, C.-T. Liao, J. L. Ellis, D. Zusin, C. Gentry, Q. L. Nguyen, J. M. Shaw, A. Picón, L. Plaja, H. C. Kapteyn, M. M. Murnane, C. Hernández-García, Controlling the polarization and vortex charge of attosecond high-harmonic beams via simultaneous spin–orbit momentum conservation. *Nat. Photonics* **13**, 123–130 (2019).
9. M. Liu, P. Huo, W. Zhu, C. Zhang, S. Zhang, M. Song, S. Zhang, Q. Zhou, L. Chen, H. J. Lezec, A. Agrawal, Y. Lu, T. Xu, Broadband generation of perfect Poincaré beams via dielectric spin-multiplexed metasurface. *Nat. Commun.* **12**, 2230 (2021).
10. R. C. Devlin, A. Ambrosio, N. A. Rubin, J. P. B. Mueller, F. Capasso, Arbitrary spin-to–orbital angular momentum conversion of light. *Science* **358**, 896–901 (2017).
11. X. Cai, J. Wang, M. J. Strain, B. Johnson-Morris, J. Zhu, M. Sorel, J. L. O'Brien, M. G. Thompson, S. Yu, Integrated compact optical vortex beam emitters. *Science* **338**, 363–366 (2012).
12. Z. Shao, J. Zhu, Y. Chen, Y. Zhang, S. Yu, Spin-orbit interaction of light induced by transverse spin angular momentum engineering. *Nat. Commun.* **9**, 926 (2018).
13. P. Miao, Z. Zhang, J. Sun, W. Walasik, S. Longhi, N. M. Litchinitser, L. Feng, Orbital angular momentum microlaser. *Science* **353**, 464–467 (2016).
14. D. Naidoo, F. S. Roux, A. Dudley, I. Litvin, B. Piccirillo, L. Marrucci, A. Forbes, Controlled generation of higher-order Poincaré sphere beams from a laser. *Nat. Photonics* **10**, 327–332 (2016).
15. C. Huang, C. Zhang, S. Xiao, Y. Wang, Y. Fan, Y. Liu, N. Zhang, G. Qu, H. Ji, J. Han, L. Ge, Y. Kivshar, Q. Song, Ultrafast control of vortex microlasers. *Science* **367**, 1018–1021 (2020).
16. W. Sun, Y. Liu, G. Qu, Y. Fan, W. Dai, Y. Wang, Q. Song, J. Han, S. Xiao, Lead halide perovskite vortex microlasers. *Nat. Commun.* **11**, 4862 (2020).
17. Z. Zhang, X. Qiao, B. Midya, K. Liu, J. Sun, T. Wu, W. Liu, R. Agarwal, J. M. Jornet, S. Longhi, N. M. Litchinitser, L. Feng, Tunable topological charge vortex microlaser. *Science* **368**, 760–763 (2020).
18. Z.-Q. Yang, Z.-K. Shao, H.-Z. Chen, X.-R. Mao, R.-M. Ma, Spin-momentum-locked edge mode for topological vortex lasing. *Phys. Rev. Lett.* **125**, 013903 (2020).
19. T. Stav, A. Faerman, E. Maguid, D. Oren, V. Kleiner, E. Hasman, M. Segev, Quantum entanglement of the spin and orbital angular momentum of photons using metamaterials. *Science* **361**, 1101–1104 (2018).
20. L. Li, Z. Liu, X. Ren, S. Wang, V.-C. Su, M.-K. Chen, C. H. Chu, H. Y. Kuo, B. Liu, W. Zang, G. Guo, L. Zhang, Z. Wang, S. Zhu, D. P. Tsai, Metalens-array–based high-dimensional and multiphoton quantum source. *Science* **368**, 1487–1490 (2020).
21. B. Chen, Y. Wei, T. Zhao, S. Liu, R. Su, B. Yao, Y. Yu, J. Liu, X. Wang, Bright solid-state sources for single photons with orbital angular momentum. *Nat. Nanotechnol.* **16**, 302–307 (2021).
22. Y. Dai, Z. Zhou, A. Ghosh, R. S. K. Mong, A. Kubo, C.-B. Huang, H. Petek, Plasmonic topological quasiparticle on the nanometre and femtosecond scales. *Nature* **588**, 616–619 (2020).
23. H. Kim, J. Park, S.-W. Cho, S.-Y. Lee, M. Kang, B. Lee, Synthesis and dynamic switching of surface plasmon vortices with plasmonic vortex lens. *Nano Lett.* **10**, 529–536 (2010).
24. K. Frischwasser, K. Cohen, J. Kher-Alden, S. Dolev, S. Tsesses, G. Bartal, Real-time sub-wavelength imaging of surface waves with nonlinear near-field optical microscopy. *Nat. Photonics* **15**, 442–448 (2021).
25. Y. Kan, S. K. H. Andersen, F. Ding, S. Kumar, C. Zhao, S. I. Bozhevolnyi, Metasurface-enabled generation of circularly polarized single photons. *Adv. Mater.* **32**, 1907832 (2020).
26. A. Pors, S. I. Bozhevolnyi, Quantum emitters near layered plasmonic nanostructures: Decay rate contributions. *ACS Photonics* **2**, 228–236 (2015).
27. T. Søndergaard, S. I. Bozhevolnyi, Surface plasmon polariton scattering by a small particle placed near a metal surface: An analytical study. *Phys. Rev. B* **69**, 045422 (2004).
28. J. Zhang, C. Sun, B. Xiong, J. Wang, Z. Hao, L. Wang, Y. Han, H. Li, Y. Luo, Y. Xiao, C. Yu, T. Tanemura, Y. Nakano, S. Li, X. Cai, S. Yu, An InP-based vortex beam emitter with monolithically integrated laser. *Nat. Commun.* **9**, 2652 (2018).
29. Y.-Y. Xie, P.-N. Ni, Q.-H. Wang, Q. Kan, G. Briere, P.-P. Chen, Z.-Z. Zhao, A. Delga, H.-R. Ren, H.-D. Chen, C. Xu, P. Genevet, Metasurface-integrated vertical cavity surface-emitting lasers for programmable directional lasing emissions. *Nat. Nanotechnol.* **15**, 125–130 (2020).
30. Y. Bao, Q. Lin, R. Su, Z.-K. Zhou, J. Song, J. Li, X.-H. Wang, On-demand spin-state manipulation of single-photon emission from quantum dot integrated with metasurface. *Sci. Adv.* **6**, eaba8761 (2020).
31. T.-Y. Huang, R. R. Grote, S. A. Mann, D. A. Hopper, A. L. Exarhos, G. G. Lopez, G. R. Kaighn, E. C. Garnett, L. C. Bassett, A monolithic immersion metalens for imaging solid-state quantum emitters. *Nat. Commun.* **10**, 2392 (2019).
32. S. K. H. Andersen, S. Kumar, S. I. Bozhevolnyi, Ultrabright linearly polarized photon generation from a nitrogen vacancy center in a nanocube dimer antenna. *Nano Lett.* **17**, 3889–3895 (2017).
33. Y.-C. Chen, B. Griffiths, L. Weng, S. S. Nicley, S. N. Ishmael, Y. Lekhai, S. Johnson, C. J. Stephen, B. L. Green, G. W. Morley, M. E. Newton, M. J. Booth, P. S. Salter, J. M. Smith, Laser writing of individual nitrogen-vacancy defects in diamond with near-unity yield. *Optica* **6**, 662–667 (2019).
34. P. R. Dolan, X. Li, J. Storteboom, M. Gu, Complete determination of the orientation of NV centers with radially polarized beams. *Opt. Express* **22**, 4379–4387 (2014).
35. J. Christinck, B. Rodiek, M. López, H. Hofer, H. Georgieva, S. Kück, Characterization of the angular-dependent emission of nitrogen-vacancy centers in nanodiamond. *Appl. Phys. B Lasers Opt.* **126**, 161 (2020).
36. L. Li, E. H. Chen, J. Zheng, S. L. Mouradian, F. Dolde, T. Schröder, S. Karaveli, M. L. Markham, D. J. Twitchen, D. Englund, Efficient photon collection from a nitrogen vacancy center in a circular bullseye grating. *Nano Lett.* **15**, 1493–1497 (2015).
37. A. Mohtashami, A. Femius Koenderink, Suitability of nanodiamond nitrogen–vacancy centers for spontaneous emission control experiments. *New J. Phys.* **15**, 043017 (2013).
38. C. Bradac, W. Gao, J. Forneris, M. E. Trusheim, I. Aharonovich, Quantum nanophotonics with group IV defects in diamond. *Nat. Commun.* **10**, 5625 (2019).
39. M. Fiorentino, F. N. C. Wong, Deterministic controlled-NOT gate for single-photon two-qubit quantum logic. *Phys. Rev. Lett.* **93**, 070502 (2004).
40. D. Istrati, Y. Pilnyak, J. C. Loredo, C. Antón, N. Somaschi, P. Hilaire, H. Ollivier, M. Esmann, L. Cohen, L. Vidro, C. Millet, A. Lemaître, I. Sagnes, A. Harouri, L. Lanco, P. Senellart, H. S. Eisenberg, Sequential generation of linear cluster states from a single photon emitter. *Nat. Commun.* **11**, 5501 (2020).
41. P. Yang, M. Yu, R. Betzholz, C. Arenz, J. Cai, Complete Quantum-State Tomography with a Local Random Field. *Phys. Rev. Lett.* **124**, 010405 (2020).
42. D. F. V. James, P. G. Kwiat, W. J. Munro, A. G. White, Measurement of qubits. *Phys. Rev. A* **64**, 052312 (2001).
43. E. Toninelli, B. Ndagano, A. Vallés, B. Sephton, I. Nape, A. Ambrosio, F. Capasso, M. J. Padgett, A. Forbes, Concepts in quantum state tomography and classical implementation with intense light: A tutorial. *Adv. Opt. Photon.* **11**, 67–134 (2019).
44. T. M. Graham, H. J. Bernstein, T.-C. Wei, M. Junge, P. G. Kwiat, Superdense teleportation using hyperentangled photons. *Nat. Commun.* **6**, 7185 (2015).
45. S. Molesky, Z. Lin, A. Y. Piggott, W. Jin, J. Vucković, A. W. Rodriguez, Inverse design in nanophotonics. *Nat. Photonics* **12**, 659–670 (2018).
46. D. Huber, M. Reindl, Y. Huo, H. Huang, J. S. Wildmann, O. G. Schmidt, A. Rastelli, R. Trotta, Highly indistinguishable and strongly entangled photons from symmetric GaAs quantum dots. *Nat. Commun.* **8**, 15506 (2017).
47. M. Prilmüller, T. Huber, M. Müller, P. Michler, G. Weihs, A. Predojević, Hyperentanglement of photons emitted by a quantum dot. *Phys. Rev. Lett.* **121**, 110503 (2018).
48. Y. Chen, M. Zopf, R. Keil, F. Ding, O. G. Schmidt, Highly-efficient extraction of entangled photons from quantum dots using a broadband optical antenna. *Nat. Commun.* **9**, 2994 (2018).
49. J. Wang, S. Paesani, Y. Ding, R. Santagati, P. Skrzypczyk, A. Salavrakos, J. Tura, R. Augusiak, L. Mančinska, D. Bacco, D. Bonneau, J. W. Silverstone, Q. Gong, A. Acín, K. Rottwitt,

L. K. Oxenløwe, J. L. O'Brien, A. Laing, M. G. Thompson, Multidimensional quantum entanglement with large-scale integrated optics. *Science* **360**, 285–291 (2018).

50. H.-S. Zhong, H. Wang, Y.-H. Deng, M.-C. Chen, L.-C. Peng, Y.-H. Luo, J. Qin, D. Wu, X. Ding, Y. Hu, P. Hu, X.-Y. Yang, W.-J. Zhang, H. Li, Y. Li, X. Jiang, L. Gan, G. Yang, L. You, Z. Wang, L. Li, N.-L. Liu, C.-Y. Lu, J.-W. Pan, Quantum computational advantage using photons. *Science* **370**, 1460–1463 (2020).

51. A. S. Solntsev, G. S. Agarwal, Y. Y. Kivshar, Metasurfaces for quantum photonics. *Nat. Photonics* **15**, 327–336 (2021).

52. E. D. Palik, *Handbook of Optical Constants of Solids* (Academic, 1985).

53. X. Guo, Y. Ding, X. Chen, Y. Duan, X. Ni, Molding free-space light with guided wave–driven metasurfaces. *Sci. Adv.* **6**, eabb4142 (2020).

54. P. Kumar, N. K. Nishchal, Self-referenced interference of laterally displaced vortex beams for topological charge determination. *Opt. Commun.* **459**, 125000 (2020).

55. J. Liu, I. Nape, Q. Wang, A. Vallés, J. Wang, A. Forbes, Multidimensional entanglement transport through single-mode fiber. *Sci. Adv.* **6**, eaay0837 (2020).

Science Advances

Room-temperature on-chip orbital angular momentum single-photon sources

Cuo WuShailesh KumarYinhui KanDanylo KomisarZhiming WangSergey I. BozhevolnyiFei Ding

View the article online
https://www.science.org/doi/10.1126/sciadv.abk3075
Permissions
https://www.science.org/help/reprints-and-permissions

Use of think article is subject to the Terms of service